Applied Surface Science 259 (2012) 747–753

Contents lists available at SciVerse ScienceDirect

Applied Surface Science

journal homepage: www.elsevier.com/locate/apsusc

Substrate-tilt angle effect on structural and optical properties of sputtered ZnO film

Hua Feng Pang[a,b], Guang An Zhang[c], Yong Liang Tang[a], Yong Qing Fu[b,*], Li Ping Wang[c], Xiao Tao Zu[a,*], Frank Placido[b]

[a] Department of Applied Physics, University of Electronic Science and Technology of China, Chengdu 610054, PR China
[b] Thin Film Centre, Scottish Universities Physics Alliance (SUPA), University of the West of Scotland, Paisley, PA1 2BE, UK
[c] State Key Laboratory of Solid Lubrication, Lanzhou Institute of Chemical Physics, Chinese Academy of Sciences, Lanzhou 730000, PR China

ARTICLE INFO

Article history:
Received 16 February 2012
Received in revised form 15 May 2012
Accepted 23 July 2012
Available online 31 July 2012

Keywords:
Sputtered ZnO film
Substrate tilt angle
Band-gap energy
Photoluminescence
New one-step method

ABSTRACT

A new one-step method utilizing a special holder for a direct current magnetron sputtering system has enabled simultaneous deposition of ZnO films with different substrate tilt angles on quartz and silicon substrates. Observation from scanning electron microscopy shows that a typical columnar structure is obtained and the column inclination angle varies from 0° to 34°. From X-ray diffraction analysis, the strains in the ZnO films decrease with increasing substrate tilt angle, which is confirmed by the variation of the longitude optical phonon vibration in the Raman spectra. The band-gap energies decrease from 3.19 eV to 3.07 eV mainly due to the changes of strain relaxation induced by the defect variations in the films. Photoluminescence spectra revealed that the generation, type and concentration of the complex defects are influenced by the substrate tilt angle.

1. Introduction

Zinc oxide (ZnO) has been widely applied for solar cell, light emitting diode, thin film transistor (TFT), surface acoustic wave (SAW) and thin film bulk acoustic wave (TFBAR) devices [1–5]. High-quality ZnO films have often been deposited using magnetron sputtering for transparent electrodes, active channel layer of TFT and piezoelectric films in SAW and TFBAR devices on semiconductor wafers [6–10]. Deposition parameters which are optimised to obtain high-quality ZnO films [4] include chamber pressure, flow ratio of the argon gas to oxygen gas, substrate temperature and sputtering power. The density distribution of the sputtered atoms and ions at different positions between the target and substrate in the sputter chamber is affected by the transfer of physical momentum and kinetic energy from the incident ions to the surface atoms [11]. Therefore, the growth rate, morphology, orientation and crystallinity of the ZnO film can be dramatically influenced by the deposited atoms impinging onto the substrate with different incident angles and energies.

Inclined ZnO films have recently received much attention because a shear wave can be excited in SAW and FBAR devices incorporating such films [4,12–14], and this results in an improvement of sensitivity of such devices for biosensing or viscosity sensing [15,16]. Inclined ZnO films have also been used in ultrasonic transducer and ultrasonic imaging, combined with the array scanning technique [17–19]. However, it is still a challenge to deposit high-quality inclined ZnO film.

Common methods used to deposit inclined ZnO films by magnetron sputtering include varying the substrate tilt angle or the angle between the substrate and target [20,21]. In this paper, we report a one-step method to deposit ZnO films with different column inclination angles using a specially designed holder. The structure and optical properties of the ZnO films deposited at different substrate tilt angles have been investigated in detail.

2. Experimental

ZnO films were deposited on quartz and silicon (1 0 0) substrates using a direct current (DC) magnetron sputter system (NS3750, Nordiko). A Zn target of 99.99% purity was used as magnetron cathode. The target dimensions are 30 cm in length, 10 cm in width and 0.6 cm in thickness. The distance of substrates from the target surface was about 15 cm, which was changed for 13–14 cm when the substrate is gradually tilted up to an angle of 60°.

Before deposition, the substrates were cleaned ultrasonically in acetone, and then fixed on a special vertical holder (see Fig. 1) allowing different tilt angles from 0° to 60° at 15° intervals in sequence. The chamber was pumped down to the base pressure of 2.2×10^{-3} Pa, then heated up to 120 °C. The samples were pre-cleaned using a bias power of 400 W in Ar atmosphere at 150 sccm

* Corresponding authors.
E-mail addresses: Richard.Fu@uws.ac.uk (Y.Q. Fu), xtzu@uestc.edu.cn (X.T. Zu).

0169-4332/$ – see front matter © 2012 Elsevier B.V. All rights reserved.
http://dx.doi.org/10.1016/j.apsusc.2012.07.114

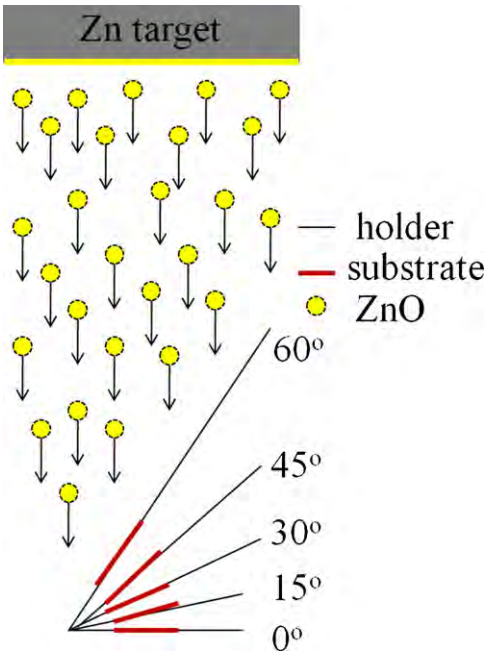

Fig. 1. Schematic image of the deposition process of the samples tilted at different angles using DC magnetic sputtering.

for 10 min. The working gas was a mixture of argon and oxygen (99.99% purity) with the optimised flow rates of the argon gas at 90 sccm and oxygen gas at 45 sccm. Pre-conditioning of the target was performed for 20 min to clean and oxidise the surface of the target to form a stable ZnO thin layer. The deposition was carried out for 3 h with a DC power of 400 W and a gas pressure of 0.64 Pa.

The ZnO films were characterised using X-ray diffraction (XRD, D5000, Siemens) with Cu Kα radiation (λ = 1.5406 Å). The surface morphologies were investigated using scanning electron microscopy (SEM, S-4100, Hitachi) and atomic force microscopy (AFM, CSPM4000, Ben-Yuan). Raman spectra were obtained using a LabRam inverted microscope spectrometer with a laser source at 532 nm (70 mW). The data processing was realised using the software LabSpec5. Optical transmittance (T) and reflectance (R) measurements were carried out using a spectrophotometer (NKD-8000, Aquila). Photoluminescence (PL) spectra were recorded at room temperature using a PL Spectrometer (LS-55, PerkinElmer).

3. Results and discussions

3.1. Microstructure and morphology

Fig. 2 shows the cross section images of the ZnO films on silicon (1 0 0) substrates deposited at different substrate-tilt angles. It can be observed that the typical columnar structure is inclined and compact, and the column inclination angles increase from 0°, 8.5°, 21°, 30° to 34° with the substrate tilt angle of 0°, 15°, 30°, 45° and 60°, respectively. This variation of column inclination angle with angle of deposition lies approximately midway between that predicted by the two most often used models of Nieuwenhuizen and Haanstra [22] and Tait et al. [23], probably because the magnetron target is far from being a point source which had also been reported by Bensmaine et al. [20]. The corresponding thicknesses are approximately 1.56, 3.59, 3.37, 2.74 and 1.59 μm, respectively, which is caused by the different incident flux of the sputtered atoms and ions on the substrates, as well as the slight difference in the distance from the target. The thickness variation of the films is dependent on the distribution of the sputtered atoms on the whole holder and the substrate tilt angle. The edge area of the holder has relatively lower deposition rate than that near the centre area due to the rectangle shape of the Zn target. Although the substrate tilt angle modulates the deposition rates of the samples, the thickness variation is mainly determined by the distribution of the sputtered atoms on the substrate. The samples tilted at 0° and 60° are thinner than those with tilt angles of 15° and 30°. The substrates of quartz and silicon were put closely in each plate, thus the thickness of the ZnO films on quartz substrates are almost equal to those on silicon substrates with different tilt angles. The lateral feature sizes of the top-view image changes with the substrate tilt angle, and clearly the growth rate, crystal features and the preferential in-plane alignment are determined by the substrate tilt angle.

Fig. 3 presents XRD patterns of the ZnO films deposited on quartz and silicon (1 0 0) substrates tilted at different angles indicating that the ZnO films have obviously preferred c-axis orientation. The intensity of the diffraction peak typically depends on film thickness, crystallinity and orientation. The intensities of the (0 0 2) peaks at 2θ near 34° increase for the ZnO films on the quartz substrates tilted at 0°, 15° and 30°, and are normalised with the corresponding thicknesses, i.e. peak intensity divided by thickness, giving 4386, 3283 and 9152 μm^{-1}, respectively. The ZnO (1 0 0) peak appears clearly in the pattern of the ZnO film on the quartz substrate inclined at 30°. However, when the tilt angle of the quartz substrate is increased to 45°, the normalised intensity data of the (0 0 2) peak decreases dramatically to 254 μm^{-1}. For the ZnO film on quartz deposited with a substrate-tilt angle of 60°, non-c-axis orientation is shown by the appearance of a (1 0 1) peak. For the ZnO films deposited on silicon substrates, the normalised intensities of the (0 0 2) peak for the samples with the substrate-tilt angle of 0° and 15° are 3922 and 2158 μm^{-1}, respectively, which are much higher than those of 45, 33 and 262 μm^{-1} obtained for substrate tilt angles of 30°, 45° and 60° respectively. The relative intensity of the (1 0 0) peak increases compared with the (0 0 2) peak on silicon with the substrate tilt angles increased from 30° to 60°, which indicates that more randomly oriented crystals exist on the film surface. The c-axis orientation of the ZnO film on silicon or quartz substrate has reduced significantly at the higher substrate tilt angles. The deterioration of the (0 0 2) orientation was considered as the results of the energy minimisation, which means the sum of the surface energy of the film, the film-substrate interface energy, and strain energy in the film keeps the smallest value during the deposition process [24,25]. When the substrate tilt angle becomes larger, the diffusion and collision among the incident plasma and atoms become significant at the surface of the deposited films. The energetic deviation of the minimum value for (0 0 2) orientation favours the other crystallographic orientation of the grain growth [24]. Based on the variation of the XRD patterns, the crystallinity and texture of ZnO films are influenced significantly by the substrate tilt angle in the deposition process.

Table 1 lists the peak shifts of the (0 0 2) peak with increase of the substrate tilt angle. The monotonous increase in the peak shifts is similar for the ZnO films on quartz substrates (from 34.02° to 34.30°) and on silicon substrates (from 34.08° to 34.32°). The strain ε in the ZnO films along c-axis can be estimated using the equation [26]:

$$\varepsilon_{film} = \frac{(c_{film} - c_{bulk})}{c_{bulk}} \quad (1)$$

where c_{film} is lattice constant of the films obtained from the position of the (0 0 2) peak, c_{bulk} is the unstrained lattice parameter of the bulk ZnO taken as 0.52069 nm [26]. The calculated results show that the maximum strain is $\sim 11.39 \times 10^{-3}$ for the ZnO films on quartz and $\sim 9.7 \times 10^{-3}$ for the ZnO film on silicon at a tilt angle of 0°. It decreases to $\sim 3.6 \times 10^{-3}$ for the ZnO film on quartz and to $\sim 2.78 \times 10^{-3}$ for the ZnO film on silicon at a tilt angle of 60°. Consideration of the linear thermal coefficients of ZnO film ($4 \times 10^{-6}\ K^{-1}$),

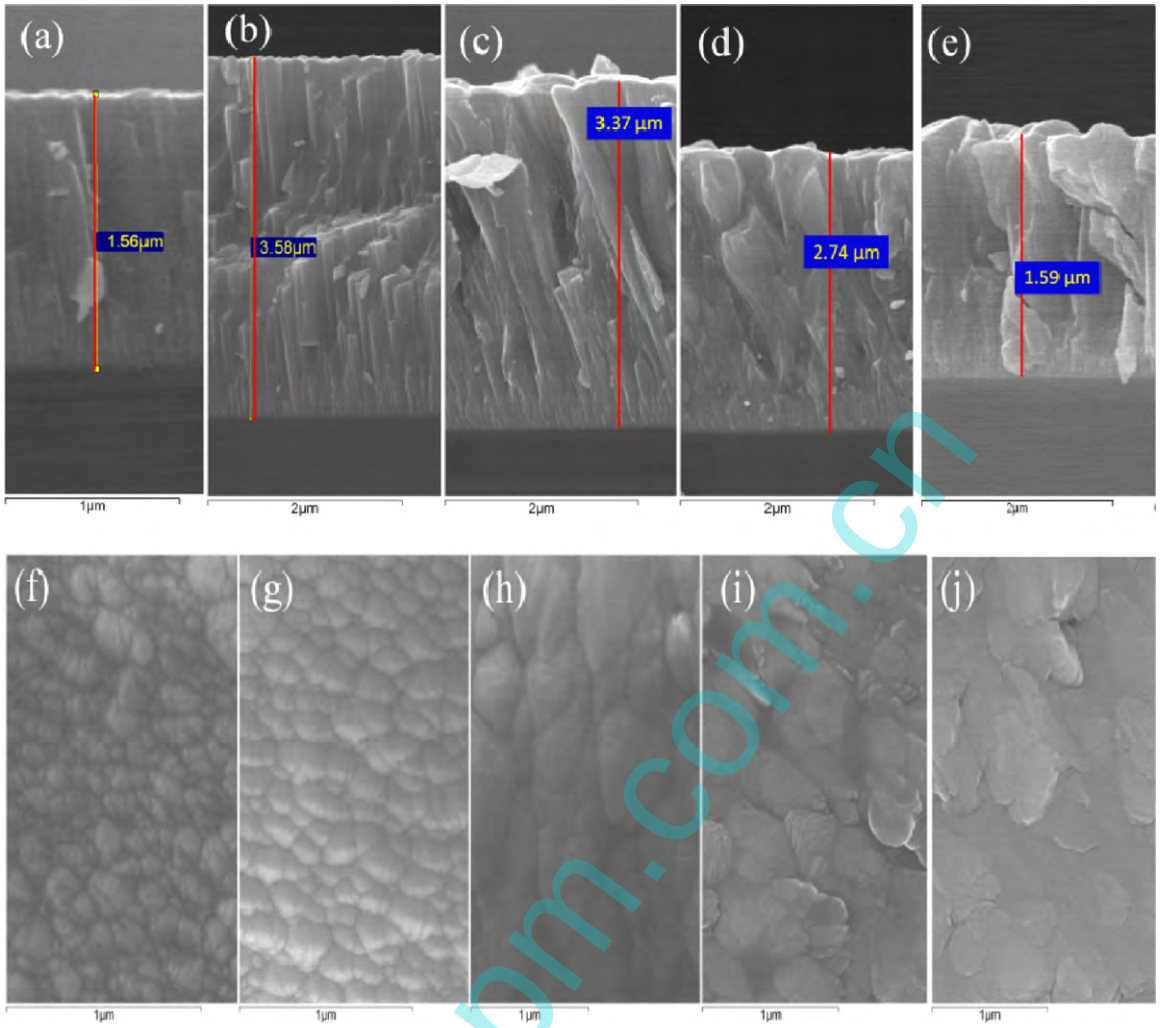

Fig. 2. SEM images of the cross section and morphologies of the ZnO film on the silicon (1 0 0) substrates tilted at different angles (a) and (f) 0°, (b) and (g) 15°, (c) and (h) 30°, (d) and (i) 45°, (e) and (j) 60°.

quartz ($0.5 \times 10^{-6}\ K^{-1}$) and silicon ($3.2 \times 10^{-6}\ K^{-1}$) implies that the strain in the ZnO films cannot be attributed to only the thermal strain of $\sim 1.55 \times 10^{-3}$ expected at the deposition temperature of 115 °C [27–29]. Therefore, the large strain is considered to arise from the growth process, which is mainly caused by the bombardment of sputtered atoms onto the substrate surface and the growing ZnO films [11,26]. The decrease of strain in ZnO films with the substrate tilt angle suggests that more defects are formed in the ZnO films with a large substrate tilt angle, releasing the film stress [30,31].

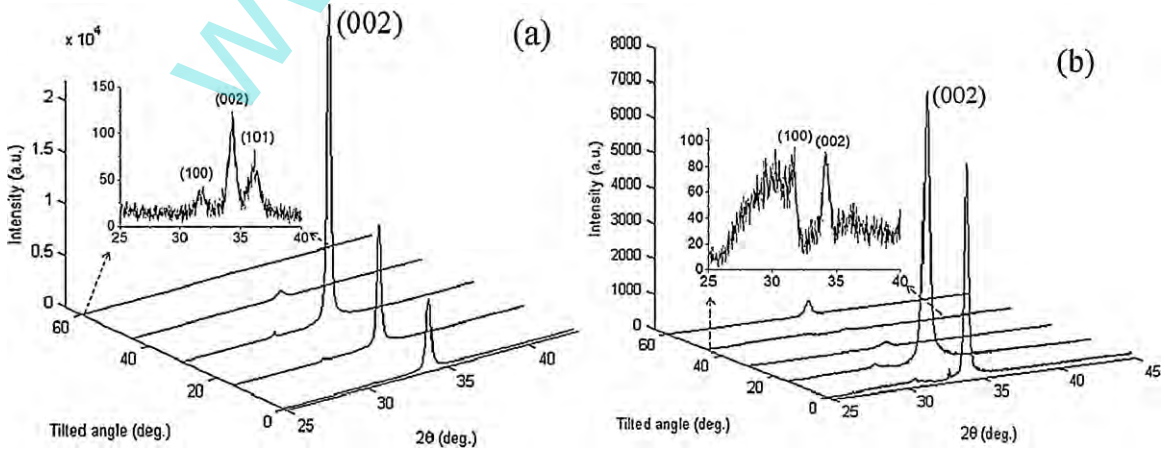

Fig. 3. XRD patterns of the ZnO film deposited on (a) quartz and (b) silicon substrates tilted at different angles, the insets of (a) and (b) are enlarged clearly for the XRD patterns of ZnO films on quartz at 60° and on silicon at 45°, respectively.

Table 1
Parameters of XRD patterns of ZnO films and corresponding substrate-tilt angle.

Sample	Sub. tilt. (°)	2θ (°)	FWHM (°)	d (nm)	c (nm)	Strain (ε_3) ($\times 10^{-3}$)
Q1	0°	34.02	0.377	0.26331	0.52662	11.39
Q2	15°	34.06	0.326	0.26301	0.52602	10.24
Q3	30°	34.08	0.275	0.26286	0.52572	9.66
Q4	45°	34.24	0.552	0.26166	0.52332	5.05
Q5	60°	34.30	0.573	0.26122	0.52244	3.36
S1	0°	34.08	0.304	0.26287	0.52574	9.70
S2	15°	34.14	0.451	0.26241	0.52482	7.93
S3	30°	34.14	0.687	0.26242	0.52484	7.97
S4	45°	34.18	0.561	0.26211	0.52422	6.78
S5	60°	34.32	0.431	0.26107	0.52214	2.78

Typical AFM images for the ZnO films on quartz deposited at different substrate tilt angles are shown in Fig. 4. The roughness was calculated using a root-mean-square average method as shown in Fig. 4f. The maximum roughness is 17.3 nm for the ZnO film with the substrate tilt angle of 30°, whilst the minimum roughness of 11.87 nm is shown for the ZnO film at the tilt angle of 15°. To compare with the roughness, the crystal sizes of the ZnO films on quartz substrates were estimated using the Debye–Scherrer formula: $D = (0.89\lambda)/[\beta\cos\theta]$, where λ, β and θ are the X-ray wavelength (1.5418 Å for Cu Kα), value of full-width at half maximum (FWHM) of the (0 0 2) peak and observed angle of the diffraction peak, respectively [32]. The grain size is determined as 21.8, 25.2, 29.9, 14.9 and 14.4 nm in sequence for the samples on quartz (see Fig. 4f). Although the lateral feature size of the compact surface morphology from the top view seems to increase with the substrate tilt angle, the microstructure of these features actually consist of lots of nanoparticles for substrate tilt angles of 45° and 60° due to the enhancement of the random growth orientation. Therefore, the surface roughness of ZnO films with substrate tilt angles of 45° and 60° decreases to 15.3 and 12.7 nm, respectively. The changes of the roughness and grain sizes of the ZnO films on quartz substrates have similar trends with those on silicon substrates, and both the maximum roughness of 17.3 nm and maximum grain size of 29.88 nm were obtained from the films with a substrate-tilt angle of 30°. For ZnO films on silicon substrates, the grain sizes range from 27.03, 18.22, 11.96, 14.65 to 19.08 nm, as shown in Fig. 4f, which are different from the variations of grain sizes of films on quartz substrates. It can be concluded that the substrate tilt angle has a vital role in the growth of inclined ZnO films by significantly changing the grain size during the deposition process. The effects of substrate orientation on the structure, column inclination angle, morphology and properties of ZnO film have previously been reported on various substrates such as (1 0 0) $SrTiO_3$, diamond and sapphire [20,33,34].

The Raman spectra of ZnO films on quartz substrates measured in backscattering mode are shown in Fig. 5. The Wurtzite form of ZnO with space group C_{4v}^6 has optical phonons including $1A_1$, $1E_1$, $2B_1$ and $2E_2$ at the Γ-point of the Brillouin zone. The $1A_1$ and $1E_1$ polar modes can be split by the macroscopic electric field [35] into a longitude optical (LO) phonon and a transverse optical (TO) phonon, thus giving the vibration modes of A_1(LO), A_1(TO), E_1(LO) and E_1(TO). The two non-polar modes of $2B_1$, are not Raman active, whilst the other non-polar modes of $2E_2$, E_2(low) and E_2(high), appear at approximately 100 and 438 cm^{-1}, respectively [36]. The asymmetrical peaks at 421 and 567 cm^{-1} can be clearly seen and are assigned to the E_2(high) and A_1(LO) modes, respectively. For the ZnO films on quartz, there are red shifts of the A_1(LO) vibration modes from 562, 565, 564, 565 to 567 cm^{-1} in sequence, which correspond to a variation of energy shift related to tensile strain [37]. A weak peak at 320 cm^{-1} appears on the ZnO film with a substrate tilt angle of 15°, corresponding to second-order Raman scattering of E_2(high)–E_2(low), and its relative intensity increases with the substrate tilt angle, probably due to local phonon vibrations of the increased defects [36,38,39]. A shoulder peak at 368 cm^{-1} is from those grains with non-*c*-axis orientation in ZnO films with substrate tilt angles of 45° and 60°, and is attributed to the A_1(TO) mode. This agrees with the appearance of the (1 0 0) peak in the XRD patterns of ZnO films with tilt angles of 45° and 60°. The peak at 590 cm^{-1}, corresponding to the E_1(LO) mode, which is absent from all our spectra, is forbidden for backscattering from the *c*-axis orientation of the ZnO film. In addition, a non-characteristic peak at 474 cm^{-1} and a shoulder peak at 505 cm^{-1} were detected for ZnO films with substrate tilt angles of 15° and 30° respectively, which could be assigned to optical phonon modes of the quartz substrate [40].

3.2. Optical properties

The optical transmittance of the samples on quartz substrates is shown in Fig. 6a demonstrating that the optical performance of the ZnO films is determined by the uniformity, structural homogeneity and crystallinity of the films. ZnO films deposited at substrate tilt angles of 0°, 15° and 30° have 70–91% optical transmission in the range of 500–1100 nm decreasing rapidly below 500 nm, especially in the ultraviolet (UV) region, due to the onset of fundamental absorption of ZnO [22]. The interference fringes become weak at higher substrate tilt angles, which are possibly originated from the scattering at the surface and absorbing in the ZnO film. Comparing with the roughness value of 17.3 nm for the ZnO film with a substrate tilt angle of 30°, the relative smaller values of the surface roughness reveal that the scattering at the surface plays a minor role on the T and R spectra for the ZnO films at higher tilt angles. The relative lower values of the T and R curves indicate the existence of a relatively strong absorption in ZnO films deposited at substrate tilt angles of 45° and 60°. The interference fringe pattern becomes weak mainly caused by defects in ZnO films which can significantly reduce the homogeneity (Fig. 6a).

Absorption edge of ZnO films deposited with higher substrate tilt angles of 45° and 60° shows a significant red-shift to the region of lower photon energy. The absorption coefficient, α, can be obtained using the following equation [29]:

$$T(\lambda) = (1 - R(\lambda))^2 e^{-\alpha(\lambda)d} \quad (2)$$

where $T(\lambda)$, $R(\lambda)$ and d are the transmittance, reflectance and thickness of the ZnO films, respectively. As a direct band-gap semiconductor, the optical band-gap energy, E_g, of ZnO can be determined from the Tauc formula [41],

$$\alpha h\nu = A(h\nu - E_g)^{1/2} \quad (3)$$

where $h\nu$ and A are the photon energy and a constant, respectively. The corresponding plots $(\alpha h\nu)^{1/2}$ versus $h\nu$ for all the ZnO films having different substrate tilt angles are shown in Fig. 6b. The optical band-gap energy E_g can be calculated from the linear portion of the band-edge region using an extrapolation method. The band-gap energies of ZnO films change from 3.19, 3.17, 3.16, 3.11 to 3.07 eV as

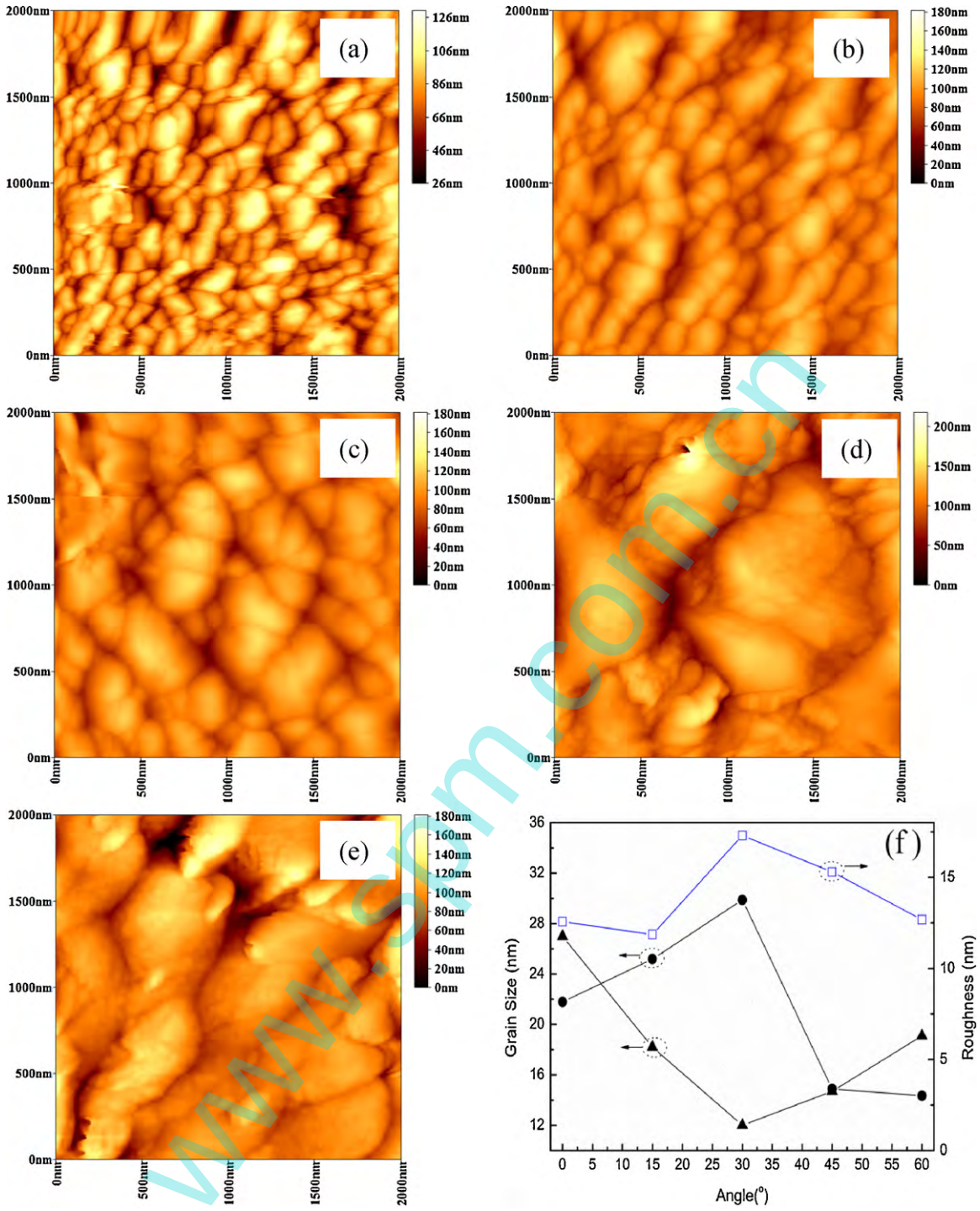

Fig. 4. AFM images of ZnO films deposited at the substrate tilt angles of (a) 0°, (b) 15°, (c) 30°, (d) 45° and (e) 60°; (f) the grain sizes of ZnO films on quartz (•), silicon (▲), and the roughness (□) of the films on quartz.

the substrate tilt angle increases from 0° to 60° in sequence. All the values of the band gap are lower than the 3.37 eV of the bulk ZnO crystal, which are caused by grain size, barriers at the grain boundary, stress and defects in the (0 0 2) orientated ZnO film [42–45]. The contribution of the grain size d to the band-gap energy can be estimated using the equation [45]:

$$\Delta E_g(d) = \frac{100}{18d^2 - 41.4d - 0.8} \quad (4)$$

The shifts of the band gap ΔE_g are calculated as 0.013, 0.010, 0.007, 0.029 eV and 0.032 eV in sequence for the different films on quartz, which implies no clear trend of the size effect. The relation of the band-gap energy to the strain of the ZnO films is shown in Fig. 7a and is linearly fitted by the following equation:

$$E_g = 3.03 + 13.81\varepsilon_{\text{film}} \quad (5)$$

The red-shift of the band-gap energy is considered to be mainly related to the decrease of strain in the films induced by defects [42]. Although the decrease of the band-gap energy with the decreasing tensile strain correlates well with the published relation between the film stress and band-gap energy [42,44], this empirical relation

does not agree with the simulation results of density functional theory based on the bulk ZnO. The theoretical result about the band gap and strain is that uniaxial stretching along the *c* axis results in a decrease in the band gap of the bulk ZnO crystal [46]. However, the difference between the nanocrystalline ZnO film and ideal bulk ZnO material is responsible for the above conflicted results. When the substrate tilt angle becomes relatively higher, the decreased strain in nanocrystal ZnO films is possibly caused by the poor crystallinity with a polycrystalline structure. Furthermore, the strain relaxation along the dislocation and grain boundary was enhanced due to the more defects at the grain boundary or inside the grain of the samples with relatively higher substrate tilt angles [42].

To further understand the variation of the defects in ZnO films, PL spectra were measured at room temperature under Xe lamp excitation of 325 nm. Fig. 7b shows the PL spectra of the as-deposited ZnO films on quartz. They basically consist of three bands as discussed below.

(1) The UV bands of two weak peaks at 378 and 391 nm (3.28 and 3.17 eV) are assigned to the band-edge transition.
(2) The multi-peak structure of the broad band, including the violet emission peak at 425 nm (2.92 eV) and blue emission peaks at 450, 460 and 486 nm are assigned to complex defects. For example, the peak at 425 nm is considered to be the result of transitions from the conduction band to deep hole trap levels like the zinc vacancy V_{Zn} [43]. The 450 and 460 nm (2.76 and 2.70 eV) emissions are assigned to electron transitions from shallow donor levels, arising from oxygen vacancies, to the valence band [47]. The sharp peak at 486 nm (2.55 eV) might originate from the lattice defects related to oxygen vacancies and zinc vacancies [48,49]. The structure of the broad band is similar to those of ZnO nano-particles and nanorods synthesised using wet chemical method [50–52].
(3) The green band, including two peaks at 530 and 554 nm (2.34 and 2.24 eV), is assigned to singly-ionised oxygen vacancies on the surface, resulting from the recombination of photo-generated holes with singly-ionised charge state [53].

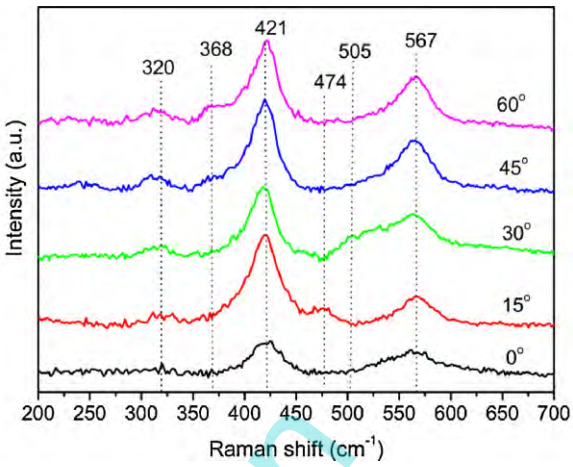

Fig. 5. Raman spectra of ZnO films deposited on quartz tilted at different angles, measured at room temperature.

Comparing the spectra of ZnO films having different columnar inclination angles, there is no UV peak observed for those films

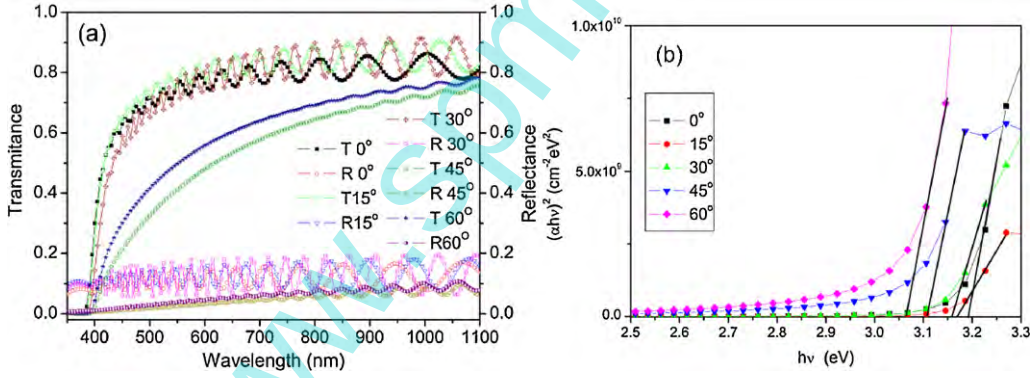

Fig. 6. (a) Optical transmittance of the ZnO films deposited on quartz substrates with different substrate-tilt angles; and (b) variation of $(\alpha h\nu)^{1/2}$ versus $h\nu$ near the absorption edge for the optical band-gap energies of ZnO films.

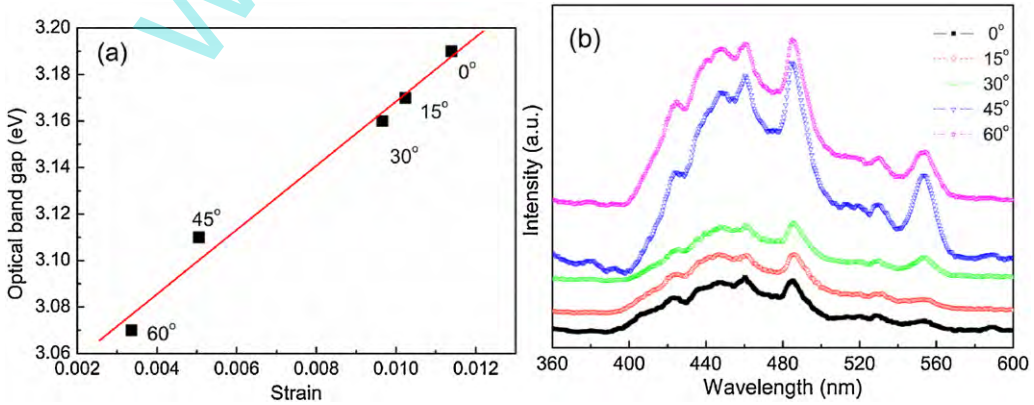

Fig. 7. (a) The band-gap energy as a function of the strain in the ZnO films with different substrate-tilt angles; (b) PL spectra of ZnO films on quartz substrates tilted at different angles.

with substrate tilt angles of 0°, 15° and 30°, but there is a weak near-band-edge emission in the spectra of those films with tilt angles of 45° and 60°. ZnO films with substrate tilt angles of 45° and 60° also show a strong emission in the blue and green bands due to the poor crystallinity with more defects in the films. These PL results suggest that the substrate tilt angle can significantly change the generation, type and concentration of the different defects in the ZnO films.

4. Conclusions

ZnO films on quartz and silicon substrates have been DC-sputtered using a new one-step method with a special holder. The SEM images show that the typical columnar structure is inclined and the column inclination angle has been changed from 0° to 34°. From the XRD analysis, the strains in the ZnO films decreased with substrate tilt angle, and this has been further elucidated from the variation of the A_1(LO) phonon vibration in the Raman spectra. The band-gap energies decreased from 3.19 eV to 3.07 eV, mainly due to the changes of strain relaxation induced by the defect variations such as the type and concentration in the ZnO film, and this have been shown to be linear with the strain in the ZnO films. The PL spectra reveal that the generation, type and concentration of the complex defects were influenced by substrate tilt angle.

Acknowledgement

This work was supported by the Fundamental Research Funds for the Central Universities (ZYGX2009J046 and ZYGX2009X007), the Sichuan Young Scientists Foundation (2010JQ0006), the Royal Society-Research Grant (RG090609), Carnegie Trust Funding, Royal Society of Edinburgh, and Royal Academy of Engineering-Research Exchanges with China and India Awards.

References

[1] H. Rensmo, K. Keis, H. Lindström, S. Södergren, A. Solbrand, A. Hagfeldt 1, S.-E. Lindquist, Journal of Physical Chemistry B 101 (1997) 2598–2601.
[2] A. Tsukazaki, M. Kubota, A. Ohtomo, T. Onuma, K. Ohtani, H. Ohno, S.F. Chichibu, M. Kawasaki, Japanese Journal of Applied Physics 44 (2005) L643–L645.
[3] R.L. Hoffman, B.J. Norrisand, J.F. Wager, Applied Physics Letters 82 (2003) 733–735.
[4] Y.Q. Fu, J.K. Luo, X.Y. Du, A.J. Flewitt, Y. Li, G.H. Markx, A.J. Walton, W.I. Milne, Sensors and Actuators B 143 (2010) 606–619.
[5] J.B. Lee, H.J. Kim, S.G. Kim, C.S. Hwang, S.-H. Hong, Y.H. Shin, N.H. Lee, Thin Solid Films 435 (2003) 179–185.
[6] A. Janotti, C.G. Van de Walle, Reports on Progress in Physics 72 (2009), 126501-1-29.
[7] O. Kluth, Thin Solid Films 351 (1999) 247–253.
[8] H.Q. Chiang, J.F. Wager, R.L. Hoffman, J. Jeong, D.A. Keszler, Applied Physics Letters 86 (2005) 013503–013505.
[9] X.Y. Du, Y.Q. Fu, S.C. Tan, J.K. Luo, et al., Applied Physics Letters 93 (2008), 094105-1-3.
[10] J.K. Luo, Y.Q. Fu, G. Ashley, W.I. Milne, Advances in Science and Technology 67 (2010) 49–58.
[11] K. Seshan, Handbook of Thin Film Deposition Processes and Techniques Principles, Methods, Equipment and Applications, 2nd ed., Noyes Publication, NJ, 2002, pp. 320–321.
[12] E. Milyutin, S. Gentil, P. Mural, Journal of Applied Physics 104 (2008), 084508-1-6.
[13] L. Qin, Q.-M. Wang, Journal of Applied Physics 108 (2010), 104510-1-9.
[14] M. Link, M. Schreiter, J. Weber, R. Gabl, D. Pitzer, R. Primig, W. Wersing, M.B. Assouar, O. Elmazria, Journal of Vacuum Science and Technology A 24 (2006), 218-1-5.
[15] M. Nirschl, A. Rantala, K. Tukkiniemi, S. Auer, A.-C. Hellgren, D. Pitzer, M. Schreiter, I. Vikholm-Lundin, Sensors 10 (2010) 4180–4193.
[16] L. Qin, Q. Chen, H. Cheng, Q. Chen, J.-F. Li, Q.-M. Wang, Journal of Applied Physics 110 (2011), 094511-1-11.
[17] M. Link, M. Schreiter, J. Weber, R. Gabl, D. Pitzer, R. Primig, W. Wersing, M.B. Assouar, Journal of Vacuum Science and Technology A 24 (2006) 218–222.
[18] T. Yanagitani, N. Morisato, S. Takayanagi, M. Matsukawa, Y. Watanabe, IEEE Transactions on Ultrasonics, Ferroelectrics, and Frequency Control 58 (2011) 1062–1068.
[19] G.-H. Feng, C.C. Sharp, Q.F. Zhou, W. Pang, E.S. Kim, K.K. Shung, Journal of Micromechanics and Microengineering 15 (2005) 586–590.
[20] S. Bensmaine, L. Le Brizoual, O. Elmazria, J.J. Fundenberger, B. Benyoucef, Physica Status Solidi (a) 204 (2007) 3091–3095.
[21] Y.E. Lee, S.G. Kim, Y.J. Kim, H.J. Kim, Journal of Vacuum Science and Technology A 15 (1997) 1194.
[22] M. Nieuwenhuizen, H.B. Haanstra, Philips Technical Review 27 (1966) 87–91.
[23] R.N. Tait, T. Smy, M.J. Brett, Thin Solid Films 226 (1993) 196–201.
[24] S.V. Prasada, S.D. Walckb, J.S. Zabinski, Thin Solid Films 360 (2000) 107–117.
[25] J.B. Lee, S.H. Kwak, H.J. Kim, Thin Solid Films 423 (2003) 262–326.
[26] X.Y. Li, H.J. Li, Z.J. Wang, H. Xia, Z.Y. Xiong, J.X. Wang, B.C. Yang, Optics Communication 282 (2009) 247–252.
[27] E. Bacaksiz, S. Yılmaz, M. Parlak, A. Varilci, M. Altunbas, Journal of Alloys and Compounds 478 (2009) 367–370.
[28] H. Watanabe, N. Yamada, M. Okaji, International Journal of Thermophysics 25 (2004) 221–236.
[29] S. Singh, R.S. Srivivasa, S.S. Major, Thin Solid Films 515 (2007) 8718–8722.
[30] P. Pant, J.D. Budai, J. Narayan, Acta Materialia 58 (2010) 1097–1103.
[31] Q.P. Wang, D.H. Zhang, H.L. Ma, X.H. Zhang, X.J. Zhang, Applied Surface Science 220 (2003) 12–18.
[32] A.L. Patterson, Physical Review 56 (1939) 978–982.
[33] M. Peruzzi, J.D. Pedarnig, D. Bäuerle, W. Schwinger, F. Schäffler, Applied Physics A 79 (2004) 1873–1877.
[34] B.H. Kong, H.K. Cho, Journal of Materials Research 22 (2007) 937–942.
[35] R.H. Callender, S.S. Sussman, M. Selders, R.K. Chang, Physical Review B 7 (1973) 3788–3798.
[36] C.F. Klingshirn, B.K. Meyer, A. Waag, A. Hoffmann, J. Geurts, Zinc Oxide: From Fundamental Properties Towards Novel Applications, Springer, Heidelberg Dordrecht London NewYork, 2010, pp. 17–26.
[37] C.P. Li, B.H. Yang, X.C. Wang, F. Wang, M.J. Li, L. Sua, X.W. Li, Applied Surface Science 257 (2011) 5998–6003.
[38] T.C. Damen, S.P.S. Porto, B. Tell, Physical Review 142 (1966) 570–574.
[39] M. Rajalakshmi, A.K. Arora, B.S. Bendre, S. Mahamuni, Journal of Applied Physics 87 (2000), 2445-1-4.
[40] K.J. Kingma, R.J. Hemley, American Mineralogist 79 (1994) 269–273.
[41] J. Tauc, A. Menth, D.L. Wood, Physical Review Letters 25 (1970) 749–752.
[42] Y.F. Li, B. Yao, Y.M. Lu, C.X. Cong, Z.Z. Zhang, Y.Q. Gai, C.J. Zheng, B.H. Li, Z.P. Wei, D.Z. Shen, X.W. Fan, L. Xiao, S.C. Xu, Y. Liu, Applied Physics Letters 91 (2007), 021915-1-10.
[43] B. Lin, Z. Fu, Y. Yia, Applied Physics Letters 79 (2001) 943–945.
[44] Y.Q. Gao, J.H. Ma, Z.M. Huang, Y. Hou, J. Wu, J.H. Chu, Applied Physics A 98 (2010) 129–134.
[45] Y. Masuda, M. Yamagishi, W.S. Seo, K. Koumoto, Crystal Growth and Design 8 (2008) 1503–1508.
[46] S.K. Yadav, T. Sadowski, R. Ramprasad, Physical Review B 81 (2010), 144120-1-5.
[47] D.H. Zhang, Z.Y. Xue, Q.P. Wang, Journal of Physics D: Applied Physics 35 (2002) 2837–2840.
[48] A.B. Djurišić, W.C.H. Choy, V.A.L. Roy, Y.H. Leung, C.Y. Kwong, K.W. Cheah, T.K. Gundu Rao, W.K. Chan, H.F. Lui, C. Surya, Advanced Functional Materials 14 (2004) 856–864.
[49] J.Q. Hu, X.L. Ma, Z.Y. Xie, N.B. Wong, C.S. Lee, S.T. Lee, Chemical Physics Letters 344 (2001) 97–100.
[50] S. Tachikawa, A. Noguchi, T. Tsuge, M. Hara, O. Odawara, H. Wada, Materials 4 (2011) 1132–1143.
[51] G.H. Du, F. Xu, Z.Y. Yuan, G. Van Tendeloo, Applied Physics Letters 88 (2006), 243101-1-3.
[52] S.S. Warule, N.S. Chaudhari, J.D. Ambekar, B.B. Kale, M.A. More, ACS Applied Materials & Interfaces 3 (2011) 3454–3462.
[53] K. Vanheusden, W.L. Warren, C.H. Seager, D.R. Tallant, J.A. Voigt, B.E. Gnade, Journal of Applied Physics 79 (1996) 7983–7990.